applied sciences

MDPI

Article

OmniSR-M: A Rock Sheet with a Multi-Branch Structure Image Super-Resolution Lightweight Method

Tianyong Liu [1], Chengwu Xu [1,*], Lu Tang [1], Yingjie Meng [1], Weijia Xu [1,2], Jinhuan Wang [1] and Jian Xu [1]

[1] Institute of Unconventional Oil & Gas Research, Northeast Petroleum University, Daqing 163318, China; lty@stu.nepu.edu.cn (T.L.)
[2] Research Institute of Exploration and Development, Daqing Oilfield Company Ltd., Daqing 163453, China
* Correspondence: xuchw@nepu.edu.cn

Abstract: With the rapid development of digital core technology, the acquisition of high-resolution rock thin section images has become crucial. Due to the limitation of optical principles, thin section imaging involves a contradiction between resolution and field of view. In order to solve this problem, this paper proposes a lightweight, fully aggregated network with multi-branch structure for super resolution of rock thin section images. The experimental results on the rock thin section dataset demonstrate that the improved method, called OmniSR-M, achieves significant enhancement compared to the original OmniSR method and also surpasses other state-of-the-art methods. OmniSR-M effectively recovers image details while maintaining its lightweight nature. Specifically, OmniSR-M reduces the number of parameters by 26.56% and the computation by 27.66% compared to OmniSR. Moreover, this paper quantitatively analyzes both the facies porosity rate and grain size features in the application scenario. The results show that the images generated by OmniSR-M successfully recover key information about the rock thin section.

Keywords: deep learning; rock thin section image; lightweight neural networks; super-resolution reconstruction

check for updates

Citation: Liu, T.; Xu, C.; Tang, L.; Meng, Y.; Xu, W.; Wang, J.; Xu, J. OmniSR-M: A Rock Sheet with a Multi-Branch Structure Image Super-Resolution Lightweight Method. *Appl. Sci.* **2024**, *14*, 2779. https://doi.org/10.3390/app14072779

Academic Editor: Atsushi Mase

Received: 5 January 2024
Revised: 13 February 2024
Accepted: 14 February 2024
Published: 26 March 2024

Copyright: © 2024 by the authors. Licensee MDPI, Basel, Switzerland. This article is an open access article distributed under the terms and conditions of the Creative Commons Attribution (CC BY) license (https://creativecommons.org/licenses/by/4.0/).

1. Introduction

Rock thin sections are an important research object in the field of geology. Geologists can determine the type, composition, and structure of rocks and reveal the conditions and processes of rock formation by observing the texture, color, and shape of the thin sections. In addition, the development of rock pores and throats can be obtained via thin sections, which in turn can be used to evaluate the storage capacity of oil and gas reservoirs. A rock thin section is a sample prepared by cutting a rock sample to a thickness of about 30 microns and going through preparatory steps such as grinding and polishing; the thin section is then observed and analyzed using an optical or electron microscope. However, the acquisition of rock thin section images is constrained by imaging equipment, leading to a trade-off between the field of view and resolution. To overcome this limitation, super-resolution reconstruction technology is considered a viable solution.

Traditional interpolation methods generally improve the resolution of an image by interpolating between pixels, but this method is more suitable for smoothing images. When dealing with images containing high-frequency information, image blurring and distortion occur because traditional interpolation methods mainly focus on color smoothing between pixels, ignoring high-frequency information such as edges and details. The problem has been effectively mitigated since a single-image super-resolution method based on a deep learning approach was proposed [1]. High-frequency information can be well preserved by introducing deep learning methods, which are widely used in nature images, medical images, satellite aerial images, military fields, and robotics [2–5]. This is also true in the field of geophysics [6–10]. However, the traditional pixel loss function in deep learning

methods often results in the generated images looking too smooth and lacking details, which predisposes them to being less capable of reconstructing texture in high-frequency images such as thin slices. In order to solve this problem, some studies have proposed super-resolution methods based on perceptual loss [11–16], but since this class of methods focuses more on improving the quality of human-perceived images, it is more applicable to natural images.

The attention mechanism is better able to capture the details of the image [17], its structure, and its texture information, focusing more on pixel-level reconstruction. In order to achieve aggregation in both spatial and channel dimensions, omnidirectional self-attention is proposed for fully aggregated networks, which realizes the full fusion of multi-scale features, including local, mid-range, and global scales [18]. Therefore, this paper proposes a lightweight super-resolution method for fully aggregated networks with multi-branch structure, comparing several state-of-the-art super-resolution methods [16,18–21], and quantitatively evaluates them in terms of structural similarity, peak signal-to-noise ratio, and perceptual quality. In addition, this paper starts from the application of thin section images and proposes the use of the large model Segment Anything (SAM) for semantic segmentation to compute the granularity information and compare it with high-definition images in order to assess the quality of the model's restoration at the edges of the grains [22]. The traditional threshold segmentation method for extracting the facies porosity rate was also used as a way of comparing the effectiveness of different algorithms.

In this work, the main contributions can be summarized as follows:

1. We propose a full aggregation network structure with a multi-branch structure, including a spatial attention mechanism and channel attention mechanism, which can learn the features of different scales better than the inherent full aggregation network structure.
2. The Omni-M method achieves a lighter weight in terms of Model FLOPs and Model Params by 27.66% and 26.56%, respectively, compared to the intrinsic method.
3. For the first time, the use of the conducted large-model SAM method is proposed for application to particle size analysis of rock thin sections, and it is proposed that the super-resolution results be evaluated through two application scenarios, namely, facies porosity rate and grain size.

2. Materials and Methods

2.1. Dataset

The dataset for this paper was derived from cores from 21 wells in the Xinjiang region, totaling 650 sheets comprising 430 sheets with a resolution of 2580 × 1944, and 220 sheets with a resolution of 4080 × 3072. All low-resolution images used for training were obtained by downsampling HR by a factor of 4. The dataset was randomly divided into two parts, with 520 images in the training set and 130 images in the test set. All the training and testing processes of this experiment were run on NVIDIA Tesla V100 GPUs, and PyTorch was used to implement the network structure of this paper.

2.2. Attention Mechanisms

Attention mechanisms include the spatial attention mechanism and the channel attention mechanism [23,24], both of which have been widely used in super-resolution tasks to improve the quality of image reconstruction since they were proposed.

The channel attention mechanism focuses on measuring the importance of each channel and dynamically adjusting the importance of each channel to highlight the more important ones, thus improving the reconstruction quality. The schematic diagram of the channel attention mechanism is shown in Figure 1. In this process, the model learns to obtain a weight vector that assigns different weights to different channels of the input feature map. These weights can be applied to the feature mapping on each channel to enhance or suppress the information on a particular channel. The implementation of the

channel attention mechanism is usually calculated using global average pooling or global maximum pooling [25], and the calculation process can be expressed as follows:

$$Z(c) = AvgPool(X(c)) \tag{1}$$

where $Z(c)$ is the feature statistic of the cth channel, $AvgPool$ denotes the global average pooling operation, and $X(c)$ denotes the cth channel of the input feature map.

$$W(c) = \sigma(F(Z(c))) \tag{2}$$

where $W(c)$ is the weight of the cth channel, F denotes a fully connected layer including the activation function, and σ denotes the activation function.

$$Y(c) = W(c) \cdot X(c) \tag{3}$$

where $Y(c)$ is the adjusted feature map of the cth channel, $W(c)$ is the weight of the corresponding channel, and $X(c)$ is the cth channel of the input feature map.

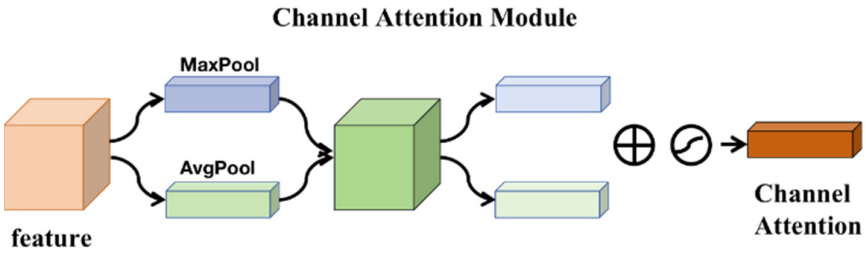

Figure 1. Channel attention mechanism.

Spatial attention mechanisms are different from channel attention mechanisms in that they focus more on the "where?", which can better capture the dependencies between pixels, provide global contextual information, and provide a larger sensory field. It allows the model to focus on different areas of the input image when generating high-resolution images to better capture details and textures. The structure of the spatial attention mechanism is shown in Figure 2. Different from the channel attention mechanism, the spatial attention mechanism will first calculate the positional energy score then convert the energy score into weights, usually using the SoftMax function to ensure that the sum of the weights is 1, thus forming a probability distribution [26]. The computational process of the spatial attention mechanism can be expressed as follows:

$$E(i,j) = F(X(i,j)) \tag{4}$$

where $E(i,j)$ is the energy fraction at location (i,j) and F is a learnable function that usually includes a convolutional layer and an activation function.

$$W(i,j) = \frac{e^{E(i,j)}}{\sum_{k,l} e^{E(k,l)}} \tag{5}$$

where $W(i,j)$ is the weight at position (i,j), $E(k,l)$ is the energy at the corresponding position, and the denominator part is normalized to the energy at all positions.

$$Y(i,j) = \sum_{k,l} W(k,l) \cdot X(i+k, j+l) \tag{6}$$

where $Y(i,j)$ is the generated output, $W(k,l)$ is the weights in the weight matrix and $X(i+k, j+l)$ is the corresponding pixel or feature in the input feature map.

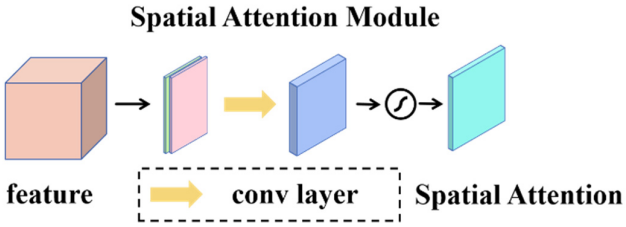

Figure 2. Spatial attention mechanism.

The channel attention mechanism and spatial attention mechanism have different focuses, and the effective integration of their respective features can help to improve the super-resolution quality of thin-film images, which has been effectively demonstrated in BAM and CBAM studies [5,10,21,23,24].

2.3. Omnidirectional Self-Attention Mechanism Module

In 2023, Wang et al. introduced a novel module called the Omnidirectional Self-Attention (OSA) mechanism [18]. Unlike the BAM and CBAM approaches, the OSA module aims to provide a more comprehensive self-attention mechanism to improve the performance of models. This attention mechanism module differs from existing self-attention mechanisms in that it considers both spatial and channel contextual information. The OSA module is able to transfer spatial and channel information compactly, which better solves the problem that important features will be distributed in different dimensions as the depth of the model deepens, and this mechanism is important for lightweight models.

The OSA module first embeds the input feature $X \in R^{HW \times C}$ into the query matrix Q^s, the key matrix K^s, and the value matrix V^s, and generates a spatial attention map (SAM) with a size of $R^{(H \times W) \times (H \times W)}$ by calculating the correlation between the query matrix Q^s and the key matrix K^s, where H, W and C are the width, height, and the channel number of the input, respectively. At this stage, a windowing strategy can be used to reduce resource overhead. Subsequently, the spatial attention map is applied to the value matrix V^s to compute the aggregated results for the spatial context, a step that typically involves multiplying the spatial attention map with the value matrix and summing the results to generate an intermediate aggregated feature map. Next, the input query matrix and key matrix are rotated to generate the transposed query matrix Q^c, the transposed key matrix K^c, and the value matrix V^c, with dimensions changed to $C \times (H \times W)$, respectively, for the channel autodidactic operation. A channel attention map of size $R^{C \times C}$ is generated by calculating the correlation between a query and a key, modeling the relationship between different channels. The channel attention map is then applied to the value matrix V^c to compute the aggregation result of the channel context. This step typically involves multiplying the channel attention map with the value matrix and summing the results to generate features of the channel context. Finally, the final aggregation result Y_{OSA} is obtained by reverse-rotating the output of the channel's self-attention, which is a tensor of size $R^{(H \times W) \times C}$ containing the output of the entire OSA block. This process can be represented as follows:

$$Q^s = X \cdot W_q \tag{7}$$

$$K^s = X \cdot W_k \tag{8}$$

$$V^s = X \cdot W_v \tag{9}$$

$$Y_s = SoftMax\left(Q^s {K^s}^T\right) \cdot V^s \tag{10}$$

where Q^s is the spatial query matrix, K^s is the spatial key matrix, V^s is the spatial value matrix, $X \in R^{HW \times C}$ denotes the input features, T is the transpose operation, Y_s is the spatial aggregation features, and $SoftMax$ is the activation function.

$$Q^c = \mathcal{R}(Q') \tag{11}$$

$$K^c = \mathcal{R}(K') \tag{12}$$

$$V^c = \mathcal{R}(V') \tag{13}$$

$$Y_c = SoftMax\left(K^c {Q^c}^T\right) \cdot V^c \tag{14}$$

$$Y_{OSA} = \mathcal{R}^{-1}(Y_c) \tag{15}$$

where Q^c is the channel query matrix; K^c is the channel key matrix; V^c is the channel value matrix; Q', K' and V' are obtained by Equations (11)–(13); $\mathcal{R}$ is the rotate operation, which is applied to Q', K', and V'; $SoftMax$ is the activation function, which will be rotated to Q^c, K^c, and V^c; Y_c is the channel aggregation feature; and Y_{OSA} is the final aggregation result.

OSA is more capable of mining deeper features compared to BAM and CBAM, which only respond to channel-wise and spatial importance without further feature information exchange. In order to fully utilize the OSA block, a more compact OSAG module is constructed to achieve multi-scale hierarchical feature extraction and obtain semantic information at multiple scales (local, mid-range, and global) for progressive receiver domain feature aggregation. The OSAG module is divided into three blocks representing local-level, medium-level, and global-level feature extraction. The local convolution block (LCB) extracts local detail information using separable convolution, etc. In the medium and global phases, Meso-OSA and Global-OSA are introduced, which use local window self-attention and sparse sampling self-attention, respectively, to obtain their corresponding semantic information. The OSAG module is able to pay better attention to different scale information, which is able to enrich the features and expand the sensory field [4].

2.4. Multi-Branch Structure

In order to make the OSAG module more lightweight and efficient while retaining the multi-scale feature information, this paper proposes the omni-scale aggregation group (OSAG) with multi-branching structure, which firstly extracts the image features using the shallow feature extraction network layers Net64, Net32, and Net16, respectively, with 64, 32, and 16 being the number of feature channels outputted from each network. The first branch is Net64, which mainly retains global semantic information, and this branch handles 64-channel feature maps. The second branch is Net32, which is responsible for aggregating local region information, and this branch processes 32-channel feature maps. The third branch is Net16, which is used to learn local details, and this branch handles 16-channel feature maps. Three branches are operated in parallel for deep feature extraction, using residual structures to splice the original shallow features and the deep features extracted through the OSAG module. Inverse convolution usually refers to transposed convolution, also known as fractional step convolution or upsampling convolution, which is a commonly used upsampling method, the principle of which is shown in Figure 3 [23,24]. In this paper, this approach is used to resize the feature map in order to fuse features of different scales to form a multi-scale feature output containing global to local features. Such a design in this paper takes full advantage of the idea of extracting multi-scale features in parallel with multiple lightweight sub-networks, which retains the multi-scale modeling capability of OSAG and improves the computational efficiency, making the OSAG module more suitable for use in lightweight and speed-critical scenarios.

Specifically, the shallow features of the image are first extracted using a multilayer 3×3 convolutional kernel, and the output feature maps are of different sizes, $64 \times H \times W$, $32 \times H \times W$, and $16 \times H \times W$, respectively. Then, the deep features on different scales are extracted separately by the OSAG module, the residual structure fuses the original shallow features, and finally, the features are fused using the inverse convolution operation. This process can be described as follows:

$$F_{64} = Conv3 \times 3(X) \tag{16}$$

$$F_{32} = Conv3 \times 3(X) \tag{17}$$

$$F_{16} = Conv3 \times 3(X) \tag{18}$$

where X is the input image and F_{64}, F_{32} and F_{16} denote the 64-channel, 32-channel, and 16-channel feature maps, respectively.

$$F'_{64} = OSAG(F_{64}) + F_{64} \tag{19}$$

$$F'_{32} = OSAG(F_{32}) + F_{32} \tag{20}$$

$$F'_{16} = OSAG(F_{16}) + F_{16} \tag{21}$$

$$F_{fusion} = Conv_{1\times1}(F'_{64}, C) + Conv_{1\times1}(F'_{32}, C) + Conv_{1\times1}(F'_{16}, C) \tag{22}$$

where, F_{64}, F_{32}, F_{16} are the feature maps extracted by the shallow network; F'_{64}, F'_{32}, F'_{16} are the deep features extracted by OSAG module; $Conv_{1\times1}$ is the 1×1 convolution, which is mainly used for adjusting the number of channels; and C is the number of required channels.

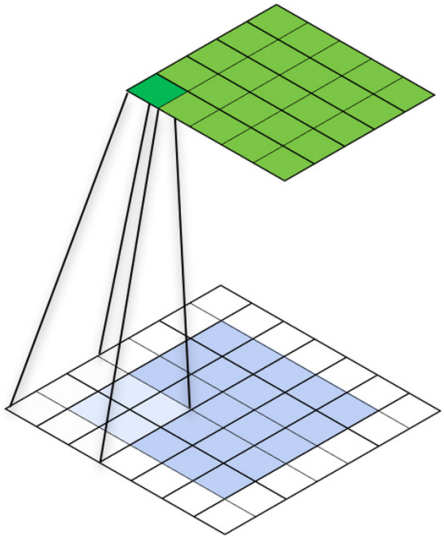

Figure 3. Schematic diagram of the inverse convolution. Blue is input (5×5), gray is the convolution kernel (3×3), green is output (5×5); padding = 1, strides = 1.

In summary, the design of OSAG modules with a multi-branch structure proposed in this paper not only improves the richness of feature representations but also makes significant progress in terms of light weight and efficiency.

2.5. Network Architecture

The overall structure of the network incorporates a multi-branch structure and clusters based on the OSA attention mechanism to develop a set of higher-performance lightweight super-resolution models. The network structure is shown in Figure 4. It mainly includes a multi-branch shallow extraction module, a deep extraction module, an inverse convolutional upsampling module, and an image reconstruction module. By inputting the LR image, the three-branch structure first extracts the shallow features, and then enters into the respective OSAG module to extract the deep features; it then performs the feature fusion after adjusting the number of channels by convolution, and finally performs the super-resolution reconstruction of the image. OSAG mainly consists of LCB, Meso-OSA, Globa-OSA Block, and Enhanced Spatial Attention (ESA) modules [18].

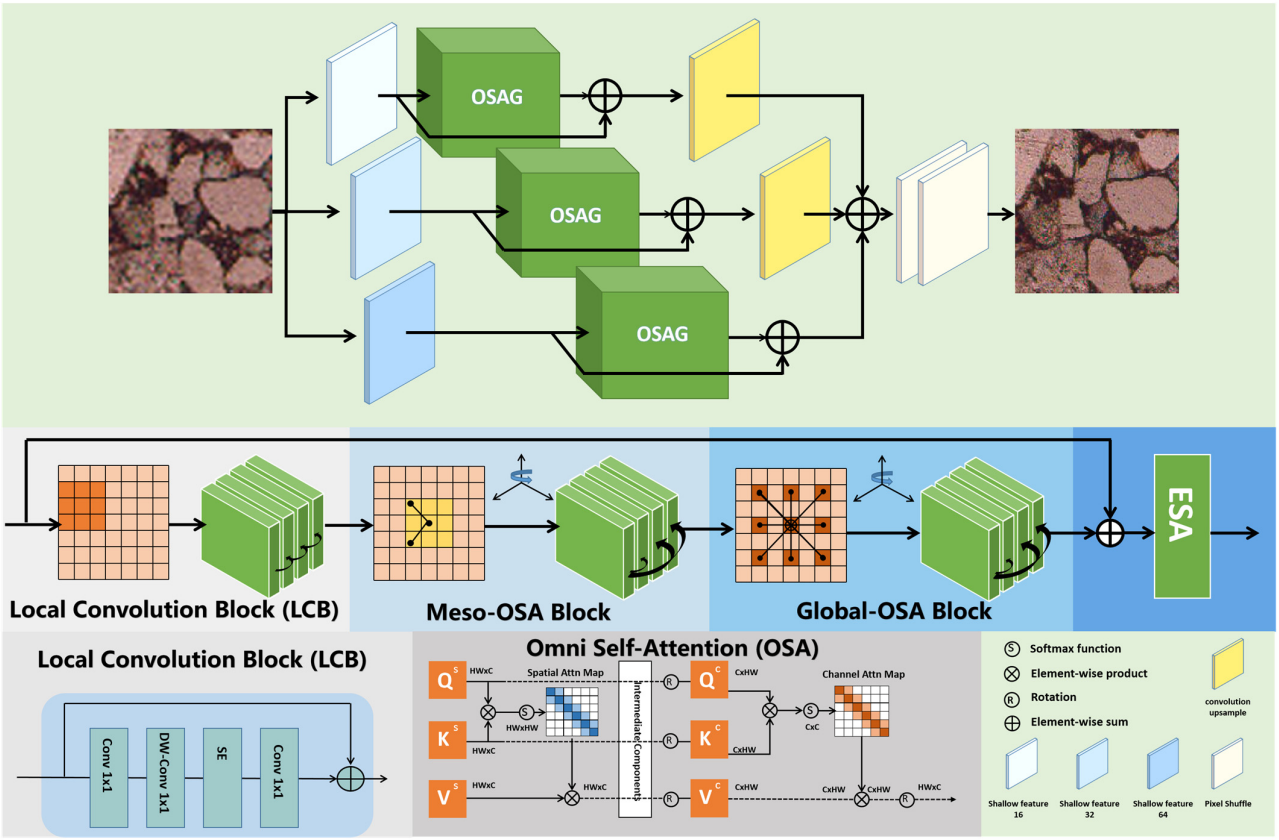

Figure 4. Fully aggregated network structure with multi-branch structure.

2.6. Loss Function

The loss function used in this paper is L_1, described by the following formula [27]:

$$L_1(I_{HR}, \hat{I}_{HR}) = \frac{1}{N}\sum_{i=1}^{N}\left|(I_{HR}(i) - \hat{I}_{HR}(i)\right| \tag{23}$$

where I_{HR} denotes a true high-resolution image and $\hat{I}_{HR}$ denotes a high-resolution image estimated by an algorithm or method.

3. Experimental Results and Their Analysis

In this section, we provide an exhaustive analysis and evaluation of the super-resolution (SR) results on the validation set. The purpose of this analysis is to gain detailed insight into the effectiveness of the proposed super-resolution technique on actual datasets. The experimental results will be explored from multiple perspectives, including comparison with state-of-the-art SR techniques, image quality assessment, aperture space segmentation effects, and thin-film granularity analysis, thus providing a comprehensive assessment of the lightweight super-resolution approach proposed in this paper.

3.1. Comparative Analysis of Different OSAG Structural Designs

In this paper, a test dataset consisting of 130 rock thin section data was used to quantitatively evaluate different OSAG structures, and the results are shown in Table 1, which mainly includes comparing the results of different OSAG layer count algorithms and the comparison of the results between different OSAG structures. As can be observed from Table 1, the performance metrics of peak signal-to-noise ratio (PSNR) and structural similarity (SSIM) experience an increasing and then decreasing trend as the number of OSAG layers increases in the OmniSR model. As the number of layers continues to increase to five, the performance decreases dramatically, indicating that too deep an OSAG

structure is not conducive to generalization. This means that increasing the number of layers can improve the feature representation of the model, but too many layers may lead to overfitting, which in turn affects the performance. Among them, OmniSR obtained a PSNR of 35.715 and an SSIM of 0.8741 at with a four-layer OSAG, a result that suggests that the four-layer OSAG seems to be a good choice for this task and dataset, enabling the best reconstruction.

Table 1. Comparative experimental results of different structural designs of OSAG modules.

Model	OSAG Number	Model FLOPs	Model Params	PSNR	SSIM
OmniSR	1	846.998 M	211.632 K	35.404	0.8716
OmniSR	2	1.423 G	356.848 K	35.317	0.8727
OmniSR	3	1.998 G	502.064 K	34.851	0.8712
OmniSR	4	2.574 G	647.280 K	35.715	0.8741
OmniSR	5	3.150 G	792.496 K	33.701	0.8492
OmniSR-M	1	1.069 G	271.600 K	35.625	0.8689
OmniSR-M	2	1.861 G	475.440 K	35.714	0.8734

In this paper, we propose that the multi-branch structural design of OmniSR-M achieves a performance close to that of a four-layer OmniSR when using only two layers of OSAG, which highlights the effectiveness of structural optimization. In addition, the new model achieves a significant improvement in reducing the computational and parametric counts by 27.66% and 26.56%, respectively, relative to the four-layer OmniSR model, an observation that highlights the importance of the trade-off between resource efficiency and performance, providing strong support for the lightweight and efficient nature of the model.

3.2. Comparison with the SOTA SR Methodology

In this paper, we evaluate performance by training several state-of-the-art super-resolution models and quantitatively evaluating them using metrics such as PSNR, SSIM, and the natural image quality evaluator (NIQE). PSNR and SSIM are important criteria commonly used to evaluate image quality and are particularly suitable for the performance evaluation of super-resolution algorithms. Based on the results of the data in Table 2, it is possible to observe the scores of the different models in terms of PSNR and SSIM. The OmniSR and OmniSR-M models performed well in terms of the highest PSNR and SSIM. The PSNR and SSIM of the OmniSR reached 35.7151 and 0.8741, respectively, and those of the OmniSR-M reached 35.7139 and 0.8734, respectively, which demonstrates their excellent ability to preserve image detail and structure. In addition, the PSNR and SSIM metrics of OmniSR-M and OmniSR are very close to each other, indicating that the multi-branch design does not degrade the reconstruction quality.

Table 2. Comparison results between advanced models.

Model	PSNR	SSIM	NIQE
ESPCN	33.4577	0.8540	7.4393
IDN	34.1920	0.8632	7.5113
RCAN	34.5803	0.8700	7.5288
RDN	35.0415	0.8728	7.5041
OmniSR	35.7151	0.8741	7.3200
OmniSR-M	35.7139	0.8734	7.1823

Using sample 0003 in Figure 5 as an example, the RCAN, Omni SR, and OmniSR-M algorithms' texture reconstruction is better, which can be seen in the break in the upper left corner; the RCAN, Omni SR, and OmniSR-M algorithms retained the break features, while the other algorithms almost ignored the break features in the upper left corner. From the quantitative metrics, the RCAN, Omni SR, and OmniSR-M achieved PNSR values of 26.52, 26.71, and 26.71, respectively.

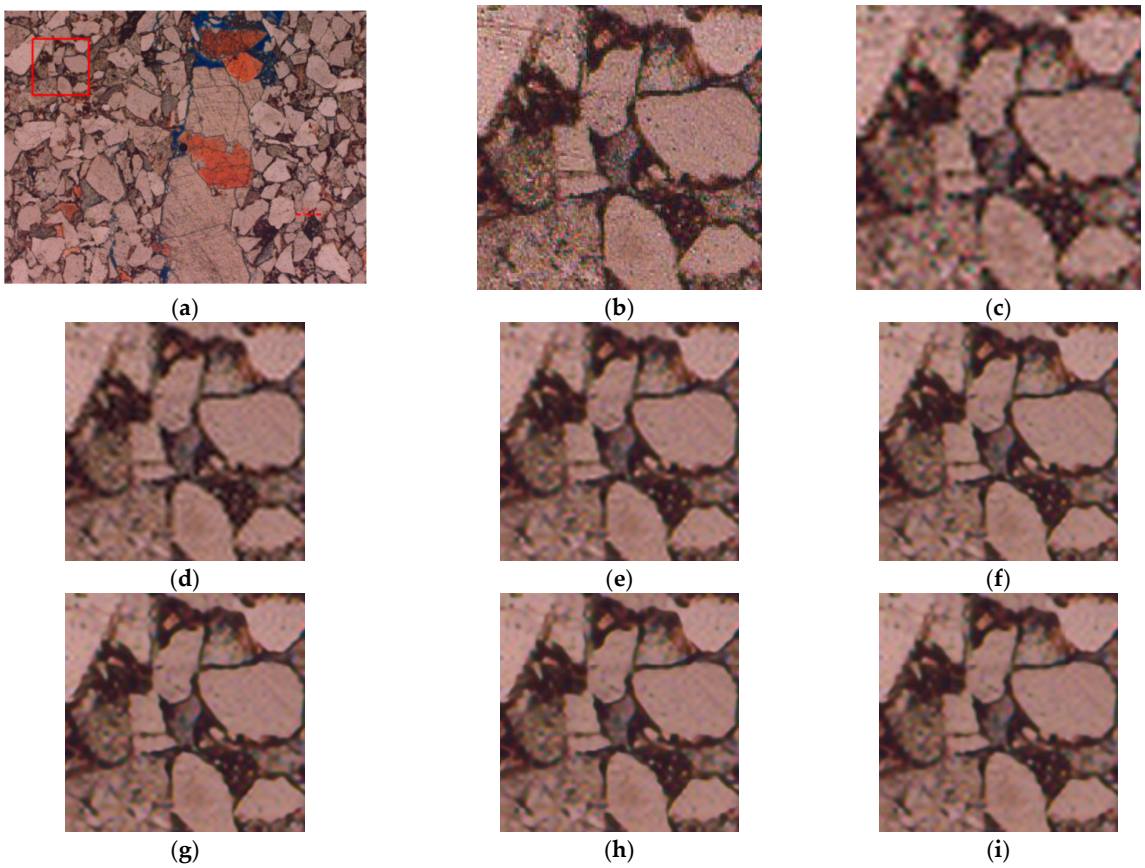

Figure 5. Individual model reconstruction results. As shown in figure, taking sample 0003 as an example, (**a**) is the original HR image of the rock thin section; (**b**) is the cropped 200 × 200 area image from the original HD image, and the red box is the sampling area; (**c**) is the LR image after downsampling by four times; (**d**) is the super-resolution result map of the ESPCN model; (**e**) is the super-resolution result map obtained by the IDN model; (**f**) is the super-resolution result map obtained by the RCAN model; (**g**) is the super-resolution result map obtained by RDN model; (**h**) is the super-resolution result map obtained by OmniSR model; and (**i**) is the super-resolution result map obtained by OmniSR-M model.

NIQE is another image quality assessment metric. Lower NIQE scores usually indicate higher image quality. From the NIQE metric, OmniSR-M achieved the lowest value of 7.1823, indicating that it generates images with the highest visual quality. The OmniSR models obtained a score of 7.3200, indicating that they also perform well in generating high-quality images. Compared to other models, OmniSR and OmniSR-M achieved optimal results on both objective and subjective metrics.

In summary, it can be concluded that the OmniSR and OmniSR-M models achieved significant performance enhancement compared to the existing models ESPCN, IDN, RCAN, and RDN, which are advanced and effective. The multi-branch structure design enables OmniSR-M to improve the subjective visual quality to a certain extent. Although it fails to surpass Omni SR in objective quantitative indexes, it has achieved similar quantitative results, which indicates that the super-resolution method with the multi-branch structure proposed in this paper has a certain degree of sophistication.

3.3. Pore Space Segmentation Analysis

To focus on a specific application scenario involving thin section images, this paper extracts the facies porosity rate of the thin section image using threshold segmentation to evaluate the reconstruction effects of different methods, Threshold segmentation is a basic image segmentation method, and its main idea is to optimize the threshold value by using

a grayscale histogram and then divide the image into different regions so that the pixels within each region have similar attributes or features [28]. In applications of thin section images for finding the facies porosity rate, threshold segmentation is used to separate the pore portion of the image from the rest of the region in order to quantify the proportion of the pore portion within the whole image. Since only a part of the region of the whole thin section image was cropped for the calculation in the experiment, it leads to a large facies porosity rate, but this does not affect the absolute error of comparing the facies porosity rate of the reconstructed images from multiple models with the HR.

In terms of the evaluation of the facies porosity rate, the rock thin section data of four samples were randomly selected in the experiment for the comparison of facies porosity rate calculation, which was 0003, 0054, 0311, and 0617, and the detailed calculation results are shown in Table 3. The HR is used as the baseline to extract the facies porosity rate, which is then compared with the porosity of the reconstruction results of each advanced super-resolution method, and the relative error is calculated to quantify the different super-resolution methods. Taking sample 0054 as an example, as shown in Figure 6, the HR facies porosity rate is 24.68%, and from the LR results, it can be seen that the downsampling caused an error in the image porosity occupancy. In contrast, Omni SR and OmniSR-M have the smallest relative errors in the facies porosity rate (24.78% and 24.72%, respectively) compared with the facies porosity rate of the original HR image.

Table 3. Comparison of relative errors of different methods of determining the facies porosity rate.

Model	Sample No. 0003		Sample No. 0311		Sample No. 0054		Sample No. 0617	
	Surface Porosity (%)	Relative Error (%)	Surface Porosity (%)	Relative Error (%)	Surface Porosity (%)	Relative Error (%)	Surface Porosity (%)	Relative Error (%)
HR	40.74	—	24.68	—	36.23	—	32.72	—
LR	41.43	0.69	24.31	−0.37	35.84	−0.39	33.89	1.17
ESPCN	42.25	1.51	24.77	0.09	36.07	−0.16	33.76	1.04
IDN	42.17	−0.08	24.82	0.14	36.28	0.05	33.7	0.98
RCAN	40.82	0.08	24.82	0.14	36.33	0.1	33.74	1.02
RDN	40.92	0.18	24.93	0.25	36.4	0.17	33.75	8.97
OmniSR	40.81	0.07	24.78	0.1	36.23	0	33.25	0.53
OmniSR-M	40.71	−0.03	24.72	0.04	36.18	−0.05	33.17	0.45

The pore occupancy results for OmniSR and OmniSR-M are closest overall to the value of HR. As in sample 0617, the pore occupancy error for the OmniSR series of models is very small and accurately recovers the value of HR. The reconstructed pore occupancy ratios of other models ESPCN, IDN, RCAN, etc. are not accurate enough and differ somewhat from the HR values. This once again validates that the OmniSR family of models can recover high-quality pore features in rock thin section image samples. The effect of multi-branch OmniSR-M was close to that of single-branch OmniSR, maintaining the accurate recovery of the pores. Test results on four samples demonstrate that the OmniSR series of models can achieve excellent performance in super-resolution applications of rock thin section pore images.

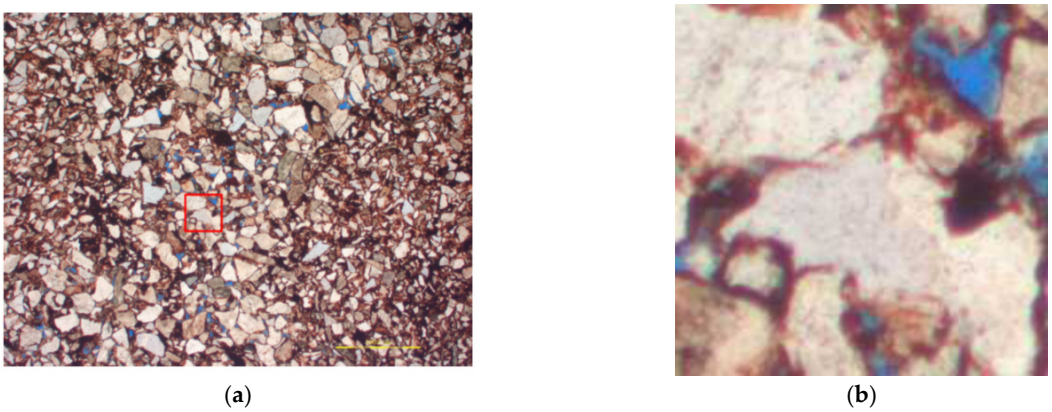

(**a**) (**b**)

Figure 6. *Cont.*

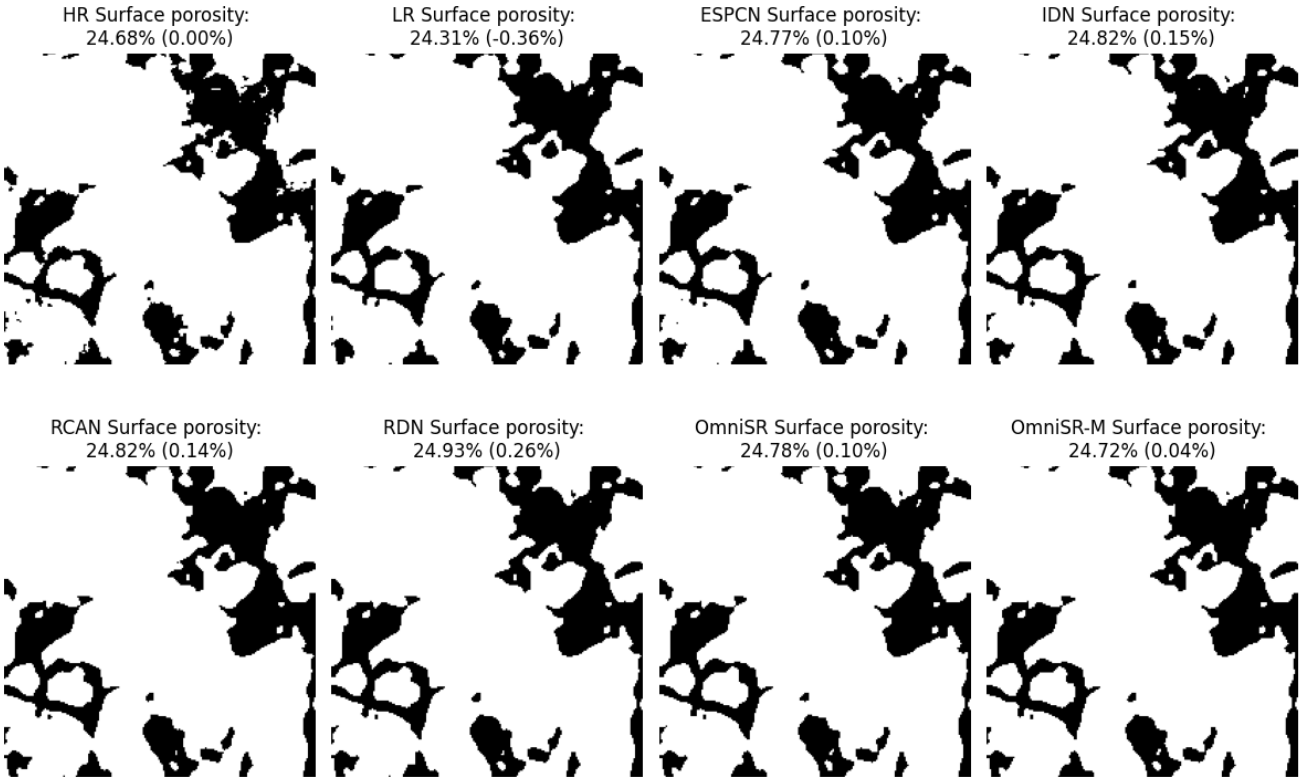

(**c**)

Figure 6. Different model reconstruction surface porosity calculation errors. (**a**) shows the original image, (**b**) shows a 200 × 200 sub-image cropped from the red boxed region, and (**c**) shows the facies porosity rate for HR, LR, and the super-resolution structure of each advanced model.

3.4. Particle Analysis

In order to better evaluate the differences between different models, this paper introduces the semantic segmentation macro model SAM to randomly select four samples to evaluate the super-resolution results of different models [22]. It is mainly used to evaluate the reconstruction of different models at the edge of the grain. As shown in Figure 7, firstly, the rock thin section grain size statistics were attained from input HR images as well as super-resolution SR maps of each model using the image method of semantic segmentation. The Udden–Wentworth particle size classification criterion (φ) was then used to plot the frequency diagram of the particle size distribution.

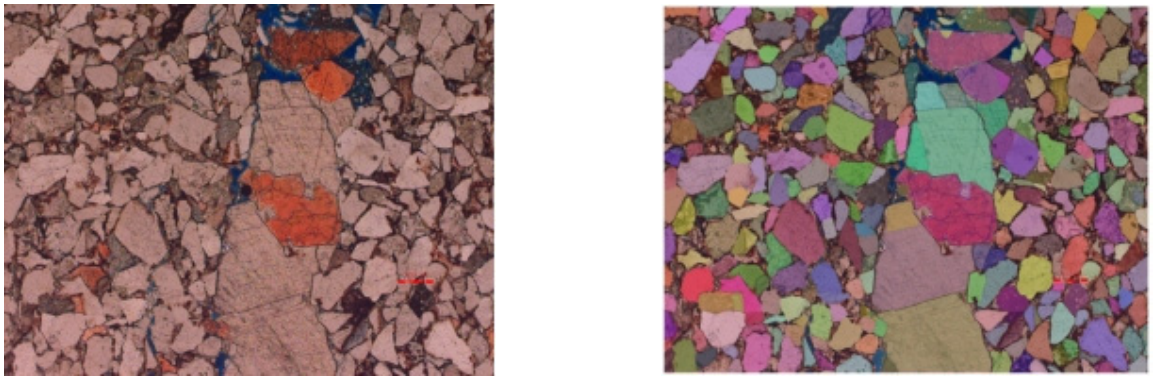

(**a**) (**b**)

Figure 7. (**a**) shows the image of input SAM, and (**b**) shows the result of semantic segmentation of SAM.

The detailed calculation results are shown in Table 4, and from the comparison results of the statistical indexes of particle size distribution in this table, it can be seen that the OmniSR-M model proposed in this paper shows significant advantages and stability in recovering the details of particle size and the overall distribution characteristics of different samples. Specifically, the recovery of the average particle size by each model is relatively close to each other; however, in the recovery of the maximum and minimum particle size ranges, OmniSR-M shows a small deviation from the true value of HR, while the other methods such as RDN show a large estimation bias, which is beyond the true range of values of HR. This indicates that OmniSR-M more accurately and completely recovers the full granularity interval contained in the image, preventing range reduction or expansion. Additionally, in terms of the particle size standard deviation, which is an indicator of the diversity of the particle size distribution, the OmniSR-M results are closest to the value of HR, implying that it recovers a degree of particle size variation that more closely approximates that of the original image, whereas the other methods are more or less guilty of omitting some of the particle size components. It should be noted that different sample images have their own particle size distribution characteristics, such as more or denser fine particle sizes, etc., but the OmniSR-M model always performs optimally and stably on all samples, which proves that it possesses strong adaptability and is able to flexibly deal with a wide range of particle size distribution situations. This can also be verified from the frequency map of particle size distribution in Figure 8, where the distribution of the OmniSR-M reconstruction results and the frequency map of HR's particle size distribution are basically the same, with the highest similarity. Finally, the metrics of OmniSR and its multi-branch structure version, OmniSR-M, almost completely overlap, which indicates that the introduction of the branch structure does not adversely affect the recovery of critical granularity details, and of its feature of light weight is thus validated.

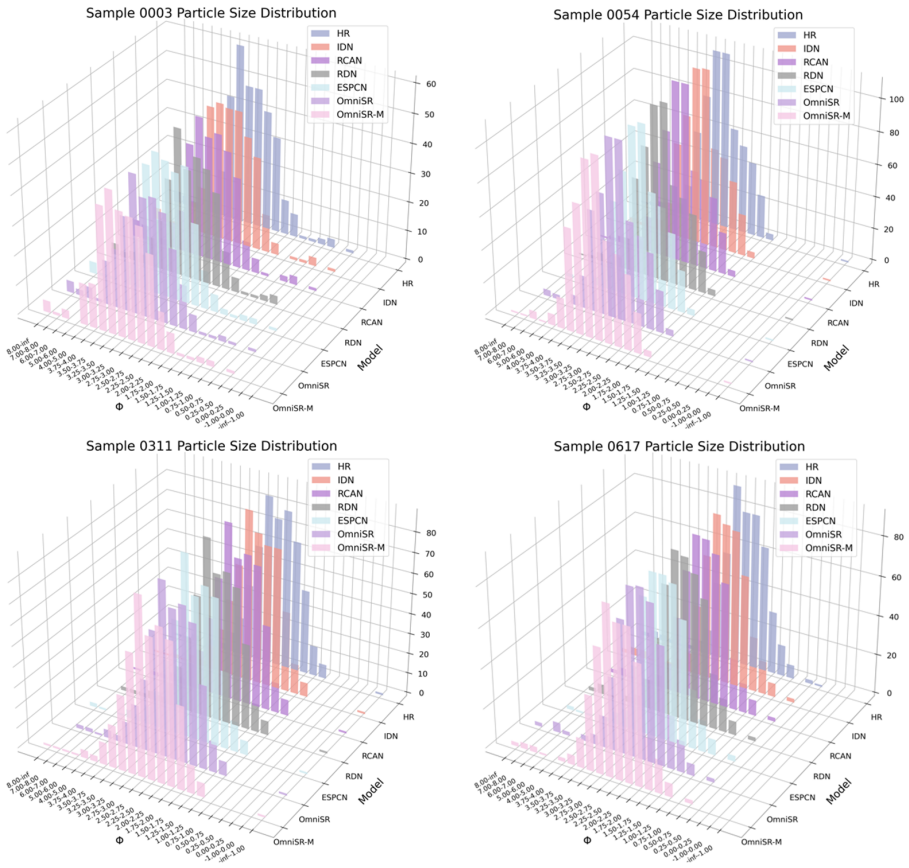

Figure 8. Frequency plot of particle size distribution for four samples.

Table 4. Quantitative results of D (particle size) and φ values for different models on four samples.

Sample No.	Model	D				φ			
		avg	max	min	std	avg	max	min	std
0003	HR	0.1353	0.7628	0.0025	0.0777	3.0961	8.6712	0.3906	0.9050
	ESPCN	0.1343	0.7592	0.0025	0.0798	3.1356	8.6712	0.3974	0.9938
	IDN	0.1318	0.7577	0.0025	0.0780	3.1577	8.6712	0.4004	0.9855
	RCAN	0.1315	0.7582	0.0017	0.0815	3.2204	9.1712	0.3993	1.1599
	RDN	0.1322	0.5579	0.0017	0.0755	3.1805	9.1712	0.8419	1.0612
	OmniSR	0.1298	0.7490	0.0017	0.0778	3.2092	9.1712	0.4170	1.0474
	OmniSR-M	0.1331	0.7616	0.0025	0.0796	3.1528	8.6712	0.3929	0.9910
0054	HR	0.1487	5.4074	0.0030	0.2249	2.9676	8.3975	−2.4349	0.7508
	ESPCN	0.1517	5.4045	0.0042	0.2265	2.9099	7.8975	−2.4342	0.6340
	IDN	0.1486	5.4057	0.0048	0.2251	2.9561	7.6899	−2.4345	0.6921
	RCAN	0.1480	5.4062	0.0024	0.2252	2.9747	8.6899	−2.4346	0.7495
	RDN	0.1482	5.4062	0.0024	0.2253	2.9763	8.6899	−2.4346	0.7608
	OmniSR	0.1487	5.4065	0.0042	0.2258	2.9645	7.8975	−2.4347	0.7345
	OmniSR-M	0.1477	5.4065	0.0038	0.2247	2.9746	8.0290	−2.4347	0.7342
0311	HR	0.2125	5.3939	0.0017	0.2450	2.4379	9.1930	−2.4313	0.7815
	ESPCN	0.2136	5.3932	0.0017	0.2461	2.4269	9.1930	−2.4311	0.7744
	IDN	0.2111	5.3934	0.0034	0.2450	2.4474	8.1930	−2.4312	0.7563
	RCAN	0.2121	5.3934	0.0024	0.2440	2.4385	8.6930	−2.4312	0.7526
	RDN	0.2107	5.3932	0.0042	0.2443	2.4535	7.9005	−2.4311	0.7710
	OmniSR	0.2120	5.3932	0.0048	0.2444	2.4383	7.6930	−2.4311	0.7473
	OmniSR-M	0.2117	5.3932	0.0034	0.2448	2.4363	8.1930	−2.4312	0.7345
0617	HR	0.2029	0.7080	0.0017	0.0878	2.4790	9.1930	0.4981	0.8907
	ESPCN	0.2080	0.8607	0.0048	0.0894	2.3962	7.6930	0.2164	0.6787
	IDN	0.2035	0.8573	0.0034	0.0900	2.4767	8.1930	0.2221	0.8941
	RCAN	0.2014	0.6497	0.0042	0.0832	2.4545	7.9005	0.6221	0.7421
	RDN	0.2016	0.6479	0.0066	0.0842	2.4590	7.2396	0.6261	0.7593
	OmniSR	0.1993	0.6484	0.0017	0.0827	2.4826	9.1930	0.6250	0.8130
	OmniSR-M	0.2026	0.8603	0.0034	0.0897	2.4710	8.1930	0.2171	0.8390

In addition, in this paper, the validity of the methods was verified on 130 test sets; specifically, the L version of SAM was used to segment the particles of all the method's super-resolution results. Subsequently, the number of particles and the particle size were computed statistically, and the detailed results of the computation are shown in Appendix A. We have also statistically visualized the number of particles in the above results, as shown in Figure 9, and the particle size information in the above results, as shown in Figure 10.

From Figure 9a, which shows the results of the super-resolution results of different methods followed by the statistics of the number of particles, it can be found that the OmniSRu method proposed in this paper is basically the same as the statistics of the other methods in terms of particle size distribution, but according to the error statistics of the number of particles of the different super-resolution methods with the HR image in Figure 9b, it can be found that the OmniSRu method had an average error of only 1.5, while the other advanced methods have an average particle number error greater than 2. This proves the effectiveness of the proposed method in this paper, and the super-resolution results are closer to those of the HR image. In analyzing these details, we observed that the average particle size curve of the OmniSRu method proposed in this paper has the highest overlap with the HR average particle size curve (according to Figure 10a and also verified in Figure 10b), where the average error of the particle size of the OmniSRu method proposed in this paper is the smallest. This indicates that the method proposed in this paper is more advanced in edge detail recovery.

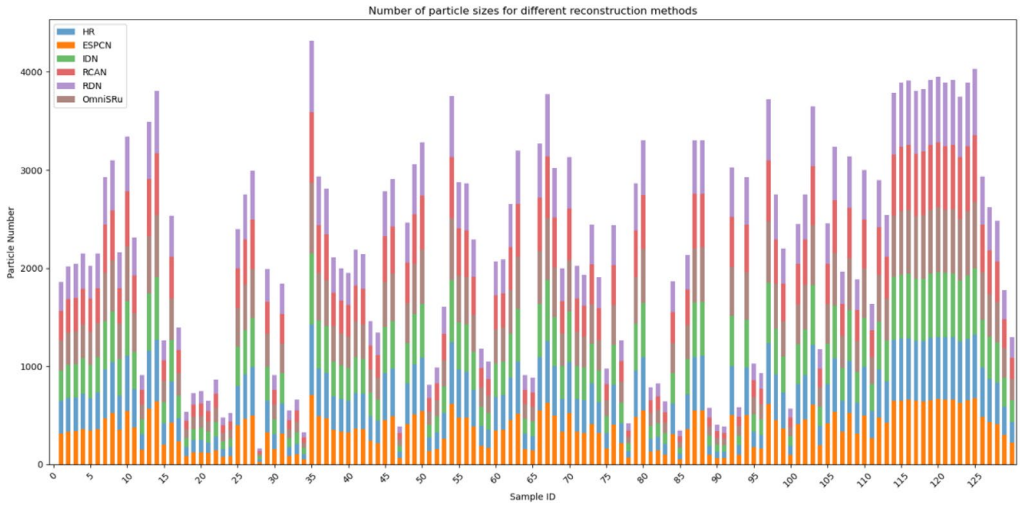

(**a**)

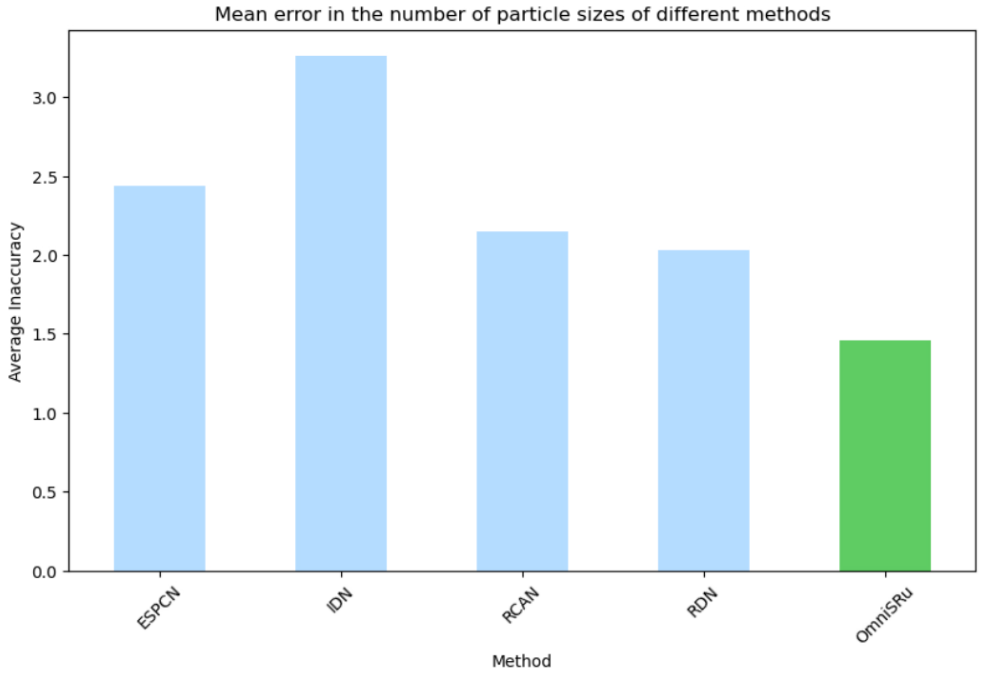

(**b**)

Figure 9. Statistical chart of the number of particles. (**a**) Number of particles for different super-resolution methods for 130 samples. (**b**) Error in the number of particles for different methods with HR.

In summary, it can be fully proven by the comprehensive granularity analysis statistical comparison results that the OmniSR-M model proposed in this paper achieves the best reconstruction results, successfully recovers the high-fidelity information of individual samples in terms of both granularity details and overall distributional features, and demonstrates its advantages in solving image super-resolution problems.

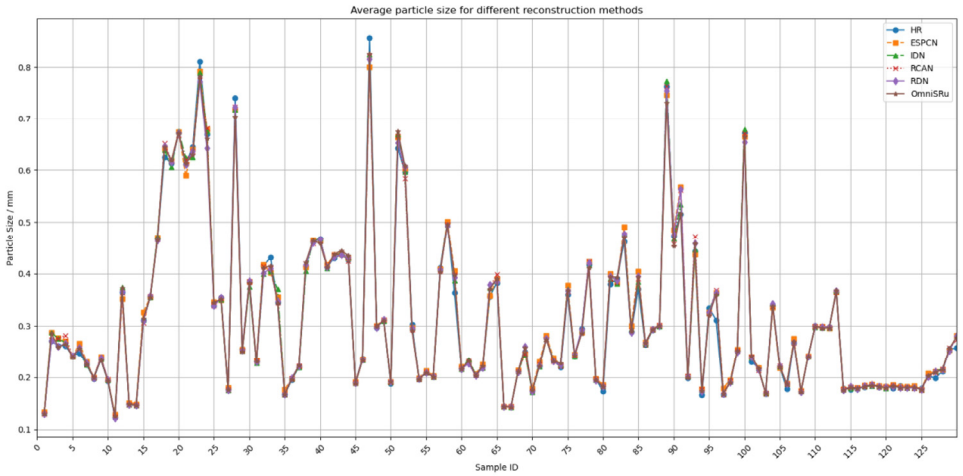

(**a**)

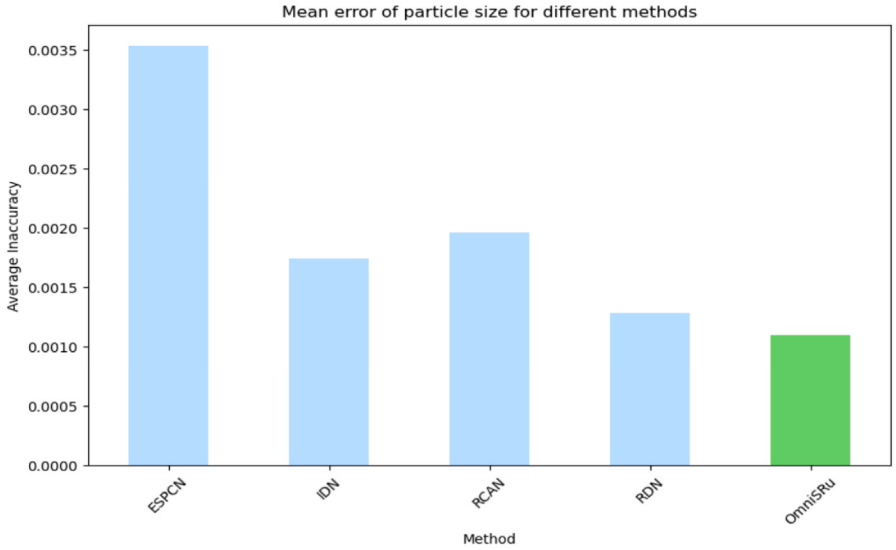

(**b**)

Figure 10. Particle size error statistical diagram. (**a**) Average particle size of 130 samples with different super-resolution methods. (**b**) Particle size error of different methods with HR.

4. Conclusions

In order to solve the conflict between field of view and resolution in rock thin section image acquisition, this paper proposes a lightweight image super-resolution network, OmniSR-M, based on omnidirectional feature aggregation with a multi-branch structure. The Omni self-attention mechanism is used to achieve synchronous interactions of spatial channel features and enhance the capability of contextual modeling. Multi-branching structures allow for the extraction of multi-scale characterizations, thereby enriching the sensory field coverage.

A large number of experimental results show that OmniSR-M obtains significant improvements in the image quality metrics of PSNR, SSIM, and NIQE, demonstrating excellent super-resolution reconstruction compared with other state-of-the-art models. Compared with the original single-branch OmniSR model, the computational and parametric quantities of OmniSR-M are reduced by 27.66% and 26.56%, respectively, meaning it is more lightweight and efficient; the training process also proves that OmniSR-M converges faster.

In addition, OmniSR-M demonstrated advanced performance in recovering key information in the rock thin section image, such as the facies porosity rate and statistical features of grain size distribution, and the reconstruction results were highly close to the original image. This proves that OmniSR-M successfully preserves the details and overall

feature information of the rock thin section image. In the experiments, we also found that OmniSR-M also had some denoising effect, and in this paper, the large model SAM was introduced for the first time to carry out particle size identification. The application of SAM in the digital rock thin section field is relatively novel, but it shows great potential. The trend in this field is leaning towards developing larger models to improve performance. Additionally work to fine-tune the SAM model for particle size identification is ongoing. In the future, we will continue to explore lightweight model designs for efficient image recovery. We hope that this work will provide valuable insights and inspiration to the rock thin section image super-resolution community.

Author Contributions: All authors contributed to the study conception and design. T.L. independently completed the study design and data analysis, while C.X. coordinated the sample data and computational resources. T.L. took the lead in writing the article, L.T. assisted in writing the article. Y.M., W.X., J.W. and J.X. proofread all drafts, and C.X. made the first guidance for the paper and all authors commented on previous versions of the manuscript. All authors have read and agreed to the published version of the manuscript.

Funding: This work was supported by the National Natural Science Foundation of China (Nos. 42172163).

Institutional Review Board Statement: Not applicable.

Informed Consent Statement: Not applicable.

Data Availability Statement: The data presented in this study are available on request from the corresponding authors, and the dataset was jointly completed by the team, so the data are not publicly available.

Conflicts of Interest: Author Weijia Xu was employed by the company Daqing Oilfield Company Ltd. The remaining authors declare that the research was conducted in the absence of any commercial or financial relationships that could be construed as a potential conflict of interest.

Appendix A

Sample ID	HR		ESPCN		IDN		RCAN		RDN		OmniSRu	
	D	Num Particles	D	Num Particles	D	Num Particles	D	Num Particles	D	Num Particles	D	Num Particles
3	0.1323	334	0.1333	312	0.1299	311	0.1295	300	0.1302	296	0.1311	307
11	0.2710	338	0.2877	334	0.2860	341	0.2739	337	0.2725	334	0.2872	331
12	0.2622	341	0.2773	340	0.2596	339	0.2763	341	0.2604	348	0.2755	338
13	0.2617	362	0.2712	360	0.2655	358	0.2817	360	0.2663	357	0.2678	351
14	0.2424	329	0.2411	345	0.2400	343	0.2413	338	0.2418	337	0.2405	335
15	0.2483	375	0.2665	359	0.2574	357	0.2575	348	0.2583	354	0.2581	353
26	0.2241	497	0.2306	471	0.2260	493	0.2260	488	0.2280	484	0.2240	493
27	0.1977	521	0.2002	522	0.1998	517	0.1987	512	0.1993	511	0.1998	515
33	0.2343	353	0.2403	351	0.2339	367	0.2369	362	0.2380	365	0.2357	364
37	0.1930	566	0.1953	542	0.1938	557	0.1965	561	0.1955	559	0.1948	557
49	0.1230	384	0.1286	381	0.1251	383	0.1240	385	0.1221	388	0.1248	390
50	0.3645	157	0.3517	153	0.3724	149	0.3633	152	0.3656	150	0.3735	148
54	0.1483	585	0.1514	573	0.1483	584	0.1476	583	0.1479	583	0.1474	586
57	0.1476	630	0.1490	640	0.1466	634	0.1457	634	0.1465	632	0.1456	635
60	0.3109	219	0.3257	202	0.3148	216	0.3059	215	0.3096	203	0.3124	212
62	0.3556	423	0.3553	423	0.3555	422	0.3568	426	0.3580	421	0.3548	420
66	0.4669	231	0.4700	238	0.4650	231	0.4661	235	0.4644	230	0.4719	230
67	0.6253	91	0.6412	88	0.6443	89	0.6519	88	0.6463	89	0.6388	90
69	0.6135	124	0.6189	122	0.6194	117	0.6170	125	0.6156	116	0.6059	121
72	0.6713	126	0.6741	123	0.6720	125	0.6681	128	0.6720	124	0.6756	119
73	0.6112	109	0.5899	116	0.6133	107	0.6196	104	0.6109	109	0.6240	106
78	0.6451	141	0.6407	141	0.6295	149	0.6362	146	0.6368	144	0.6252	146
82	0.8107	79	0.7921	81	0.7823	79	0.7757	79	0.7723	80	0.7901	80
86	0.6697	88	0.6783	87	0.6613	90	0.6810	87	0.6426	89	0.6757	86
89	0.3391	402	0.3459	397	0.3446	399	0.3386	403	0.3384	397	0.3423	397
90	0.3539	454	0.3493	462	0.3518	455	0.3533	460	0.3544	458	0.3504	461
100	0.1779	496	0.1804	498	0.1767	499	0.1766	502	0.1759	502	0.1756	499
114	0.7402	27	0.7187	28	0.7042	29	0.7235	28	0.7237	28	0.7189	27
116	0.2556	323	0.2543	327	0.2508	346	0.2519	330	0.2539	331	0.2524	332
130	0.3834	150	0.3847	157	0.3822	151	0.3844	152	0.3862	148	0.3750	152
134	0.2309	308	0.2333	312	0.2313	307	0.2318	303	0.2298	306	0.2285	306
135	0.4148	92	0.4172	86	0.4107	91	0.4135	92	0.4005	93	0.3999	93

Sample ID	HR		ESPCN		IDN		RCAN		RDN		OmniSRu	
	D	Num Particles	D	Num Particles	D	Num Particles	D	Num Particles	D	Num Particles	D	Num Particles
145	0.4312	107	0.4022	104	0.4150	116	0.4106	113	0.4101	115	0.4048	107
154	0.3446	54	0.3554	53	0.3431	63	0.3446	55	0.3474	54	0.3698	51
158	0.1670	718	0.1765	709	0.1672	723	0.1669	720	0.1669	723	0.1670	722
160	0.1951	484	0.1973	492	0.1969	492	0.1971	484	0.1992	494	0.1975	486
161	0.2201	460	0.2211	472	0.2227	476	0.2224	467	0.2219	466	0.2201	467
168	0.4136	345	0.4122	352	0.4222	353	0.4192	344	0.4169	355	0.4049	357
169	0.4612	337	0.4648	334	0.4635	339	0.4583	332	0.4595	330	0.4625	327
170	0.4674	321	0.4643	325	0.4579	334	0.4632	324	0.4664	323	0.4668	323
172	0.4125	363	0.4170	364	0.4121	367	0.4150	365	0.4121	363	0.4105	365
176	0.4304	359	0.4359	359	0.4368	355	0.4359	356	0.4327	355	0.4349	356
179	0.4355	244	0.4367	244	0.4440	243	0.4381	241	0.4356	247	0.4391	239
181	0.4266	225	0.4298	219	0.4342	215	0.4242	229	0.4316	229	0.4308	225
195	0.1909	475	0.1916	455	0.1879	471	0.1896	462	0.1893	461	0.1889	460
196	0.2368	487	0.2355	488	0.2336	485	0.2346	481	0.2352	480	0.2334	485
210	0.8565	64	0.8008	68	0.8258	60	0.8217	67	0.8149	63	0.8243	62
215	0.2969	412	0.3000	411	0.2987	412	0.2989	411	0.2967	409	0.3004	410
218	0.3110	513	0.3109	511	0.3107	512	0.3123	508	0.3119	513	0.3101	505
221	0.1881	542	0.1914	546	0.1918	552	0.1905	549	0.1916	545	0.1910	546
232	0.6424	139	0.6637	135	0.6751	131	0.6659	136	0.6531	138	0.6690	133
233	0.5970	169	0.6031	160	0.6085	162	0.5847	168	0.6060	166	0.5969	164
236	0.3029	258	0.2963	265	0.2913	268	0.2939	268	0.2959	276	0.2982	268
241	0.1964	628	0.1993	617	0.1967	635	0.1962	623	0.1973	621	0.1973	627
243	0.2103	491	0.2126	480	0.2087	478	0.2087	477	0.2097	469	0.2093	478
246	0.2038	464	0.2039	481	0.2014	482	0.2016	476	0.2023	482	0.2014	480
261	0.4117	378	0.4091	385	0.4036	385	0.4055	388	0.4075	379	0.4086	380
266	0.4989	197	0.5010	193	0.4955	199	0.4949	200	0.4930	194	0.4959	195
277	0.3635	178	0.4050	173	0.3972	172	0.3971	174	0.3922	174	0.3863	177
279	0.2171	346	0.2204	345	0.2160	340	0.2173	347	0.2165	349	0.2158	346
287	0.2300	352	0.2287	353	0.2324	343	0.2309	346	0.2268	344	0.2348	349
295	0.2055	436	0.2073	450	0.2039	442	0.2043	442	0.2031	440	0.2055	445
296	0.2223	534	0.2252	517	0.2220	533	0.2198	538	0.2187	542	0.2185	534
304	0.3562	156	0.3570	158	0.3700	150	0.3736	148	0.3787	148	0.3723	150
305	0.3823	144	0.3906	142	0.3907	152	0.3981	147	0.3840	150	0.3870	151
307	0.1442	542	0.1444	549	0.1432	544	0.1436	542	0.1434	547	0.1433	542
308	0.1441	629	0.1444	627	0.1429	625	0.1437	627	0.1435	633	0.1432	630
311	0.2125	502	0.2136	497	0.2111	504	0.2121	509	0.2107	507	0.2117	503
317	0.2506	331	0.2465	334	0.2585	335	0.2468	332	0.2607	329	0.2460	334
325	0.1736	518	0.1783	526	0.1748	518	0.1738	522	0.1733	524	0.1722	520
334	0.2223	337	0.2299	331	0.2218	337	0.2253	338	0.2229	338	0.2204	344
339	0.2778	333	0.2812	324	0.2744	329	0.2750	316	0.2762	315	0.2746	316
351	0.2336	409	0.2389	415	0.2320	407	0.2313	405	0.2317	404	0.2343	403
360	0.2194	315	0.2231	318	0.2274	321	0.2218	317	0.2242	318	0.2247	320
364	0.3599	157	0.3778	163	0.3682	169	0.3656	168	0.3666	159	0.3705	163
366	0.2412	403	0.2459	407	0.2432	411	0.2432	403	0.2454	406	0.2413	404
386	0.2944	201	0.2873	216	0.2857	215	0.2912	211	0.2927	208	0.2926	210
387	0.4167	69	0.4226	69	0.4110	75	0.4231	68	0.4200	68	0.4159	68
397	0.1974	472	0.1975	485	0.1948	475	0.1967	474	0.1945	482	0.1952	477
398	0.1727	550	0.1863	547	0.1820	550	0.1822	551	0.1824	552	0.1819	549
410	0.3794	128	0.3992	132	0.3942	135	0.3889	133	0.3945	131	0.3906	128
411	0.3904	137	0.3828	146	0.3931	139	0.3832	136	0.3866	135	0.3812	134
416	0.4615	111	0.4908	100	0.4706	107	0.4760	107	0.4767	111	0.4783	107
419	0.2889	311	0.3001	308	0.2898	313	0.2911	312	0.2874	316	0.2942	309
424	0.3706	60	0.4048	52	0.3938	59	0.3900	56	0.3951	59	0.3849	60
432	0.2641	355	0.2687	361	0.2673	358	0.2637	359	0.2681	350	0.2653	350
437	0.2919	548	0.2931	547	0.2935	554	0.2928	553	0.2930	548	0.2928	553
438	0.2998	558	0.3005	552	0.3008	548	0.3011	545	0.3004	546	0.2996	553
448	0.7626	94	0.7460	98	0.7309	102	0.7623	93	0.7552	95	0.7738	92
455	0.4726	68	0.4851	64	0.4535	69	0.4569	71	0.4755	63	0.4672	69
456	0.5148	66	0.5680	64	0.5162	67	0.5621	62	0.5633	62	0.5333	65
466	0.1993	500	0.2028	505	0.1994	506	0.2018	511	0.2018	503	0.2020	503
469	0.4425	94	0.4371	100	0.4575	99	0.4726	95	0.4582	97	0.4464	99
472	0.1663	484	0.1782	504	0.1743	483	0.1760	486	0.1733	484	0.1753	485
474	0.3347	158	0.3263	177	0.3206	179	0.3242	174	0.3259	171	0.3295	171
477	0.3112	140	0.3632	161	0.3597	160	0.3681	157	0.3638	160	0.3637	154
483	0.1676	620	0.1791	617	0.1685	620	0.1674	621	0.1684	621	0.1679	620
489	0.1922	464	0.1953	454	0.1900	467	0.1930	449	0.1900	459	0.1917	456
491	0.2523	364	0.2544	368	0.2521	368	0.2526	377	0.2507	364	0.2526	363
498	0.6718	92	0.6646	99	0.6648	95	0.6703	95	0.6548	97	0.6789	95
508	0.2307	403	0.2402	413	0.2419	406	0.2406	412	0.2391	406	0.2380	408
511	0.2181	456	0.2187	456	0.2169	464	0.2137	460	0.2150	462	0.2176	455
514	0.1687	614	0.1698	606	0.1692	607	0.1688	604	0.1706	609	0.1700	610
516	0.3388	192	0.3358	199	0.3383	198	0.3382	193	0.3426	195	0.3437	195
519	0.2199	404	0.2181	417	0.2208	408	0.2221	403	0.2219	414	0.2213	411

Sample ID	HR		ESPCN		IDN		RCAN		RDN		OmniSRu	
	D	Num Particles	D	Num Particles	D	Num Particles	D	Num Particles	D	Num Particles	D	Num Particles
521	0.1774	540	0.1882	538	0.1869	539	0.1876	537	0.1869	542	0.1873	540
527	0.2675	318	0.2754	331	0.2697	331	0.2681	333	0.2675	324	0.2704	327
531	0.1730	531	0.1743	525	0.1719	519	0.1732	513	0.1722	524	0.1729	528
533	0.2407	316	0.2417	314	0.2406	316	0.2413	314	0.2402	314	0.2408	310
535	0.2998	498	0.2989	497	0.2996	501	0.2993	496	0.2990	506	0.2985	501
537	0.2985	276	0.2993	267	0.2958	276	0.2982	275	0.2978	272	0.2963	273
538	0.2974	488	0.2955	481	0.2963	482	0.2972	482	0.2974	483	0.2973	482
541	0.3643	421	0.3645	424	0.3678	421	0.3649	422	0.3664	428	0.3668	426
545	0.1785	621	0.1777	649	0.1753	643	0.1761	625	0.1755	628	0.1764	621
547	0.1771	635	0.1812	650	0.1807	645	0.1807	655	0.1819	654	0.1792	651
551	0.1782	627	0.1804	659	0.1788	657	0.1790	660	0.1778	657	0.1785	651
552	0.1814	609	0.1847	646	0.1829	635	0.1821	637	0.1829	645	0.1821	637
569	0.1856	615	0.1870	642	0.1845	637	0.1853	645	0.1856	637	0.1835	650
571	0.1817	636	0.1831	657	0.1827	654	0.1817	660	0.1822	663	0.1827	649
573	0.1827	634	0.1820	665	0.1795	659	0.1807	660	0.1807	666	0.1794	664
577	0.1789	632	0.1864	662	0.1835	656	0.1835	648	0.1827	647	0.1839	644
584	0.1836	634	0.1818	661	0.1799	649	0.1799	655	0.1806	660	0.1806	658
593	0.1810	618	0.1826	630	0.1809	627	0.1802	627	0.1795	620	0.1803	628
600	0.1810	624	0.1836	653	0.1811	647	0.1788	660	0.1803	652	0.1801	658
603	0.1785	648	0.1770	674	0.1767	678	0.1755	678	0.1770	677	0.1763	673
617	0.2029	499	0.2080	487	0.2035	485	0.2014	487	0.2016	494	0.2026	485
618	0.1985	436	0.2110	435	0.2101	430	0.2093	441	0.2115	440	0.2113	437
636	0.2121	419	0.2145	410	0.2146	417	0.2156	415	0.2147	415	0.2172	408
647	0.2554	291	0.2536	299	0.2574	295	0.2582	299	0.2527	292	0.2544	298
648	0.2577	210	0.2816	222	0.2783	224	0.2740	218	0.2801	213	0.2791	213

References

1. Dong, C.; Loy, C.C.; He, K.; Tang, X. Learning a Deep Convolutional Network for Image Super-Resolution. In *Computer Vision—ECCV 2014*; Fleet, D., Pajdla, T., Schiele, B., Tuytelaars, T., Eds.; Lecture Notes in Computer Science; Springer International Publishing: Cham, Switzerland, 2014; Volume 8692, pp. 184–199. ISBN 978-3-319-10592-5.
2. Chen, S.; Ogawa, Y.; Zhao, C.; Sekimoto, Y. Large-Scale Individual Building Extraction from Open-Source Satellite Imagery via Super-Resolution-Based Instance Segmentation Approach. *ISPRS J. Photogramm. Remote Sens.* **2023**, *195*, 129–152. [CrossRef]
3. Nascimento, V.; Laroca, R.; Lambert, J.D.A.; Schwartz, W.R.; Menotti, D. Super-Resolution of License Plate Images Using Attention Modules and Sub-Pixel Convolution Layers. *Comput. Graph.* **2023**, *113*, 69–76. [CrossRef]
4. Sun, J.; Li, Z.-Y.; Li, P.-C.; Li, H.; Pang, X.-W.; Wang, H. Improving the Diagnostic Performance of Computed Tomography Angiography for Intracranial Large Arterial Stenosis by a Novel Super-Resolution Algorithm Based on Multi-Scale Residual Denoising Generative Adversarial Network. *Clin. Imaging* **2023**, *96*, 1–8. [CrossRef] [PubMed]
5. Xu, M.; Wang, Z.; Zhu, J.; Jia, X.; Jia, S. Multi-Attention Generative Adversarial Network for Remote Sensing Image Super-Resolution 2021.
6. Guo, C.; Gao, C.; Liu, C.; Liu, G.; Sun, J.; Chen, Y.; Gao, C. Super-Resolution in Thin Section of Lacustrine Shale Reservoirs and Its Application in Mineral and Pore Segmentation. *Appl. Comput. Geosci.* **2023**, *19*, 100133. [CrossRef]
7. Jackson, S.J.; Niu, Y.; Manoorkar, S.; Mostaghimi, P.; Armstrong, R.T. Deep Learning of Multi-Resolution X-Ray Micro-CT Images for Multi-Scale Modelling. *Phys. Rev.* **2022**, *17*, 054046.
8. Liu, Y.; Zhang, Q.; Zhang, N.; Lv, J.; Gong, M.; Cao, J. Enhancement of Thin-Section Image Using Super-Resolution Method with Application to the Mineral Segmentation and Classification in Tight Sandstone Reservoir. *J. Pet. Sci. Eng.* **2022**, *216*, 110774. [CrossRef]
9. Wang, Y.D.; Armstrong, R.T.; Mostaghimi, P. Enhancing Resolution of Digital Rock Images with Super Resolution Convolutional Neural Networks. *J. Pet. Sci. Eng.* **2019**, *182*, 106261. [CrossRef]
10. Yuan, B.; Li, H.; Du, Q. Enhancing Identification of Digital Rock Images Using Super-Resolution Deep Neural Network. *Geoenergy Sci. Eng.* **2023**, *229*, 212130. [CrossRef]
11. Kim, J.; Lee, J.K.; Lee, K.M. Accurate Image Super-Resolution Using Very Deep Convolutional Networks. In Proceedings of the IEEE Conference on Computer Vision and Pattern Recognition (CVPR), Las Vegas, NV, USA, 27–30 June 2016.
12. Ledig, C.; Theis, L.; Huszar, F.; Caballero, J.; Cunningham, A.; Acosta, A.; Aitken, A.; Tejani, A.; Totz, J.; Wang, Z.; et al. Photo-Realistic Single Image Super-Resolution Using a Generative Adversarial Network. In Proceedings of the IEEE Conference on Computer Vision and Pattern Recognition (CVPR), Honolulu, HI, USA, 21–26 July 2017.
13. Lim, B.; Son, S.; Kim, H.; Nah, S.; Lee, K.M. Enhanced Deep Residual Networks for Single Image Super-Resolution. In Proceedings of the IEEE Conference on Computer Vision and Pattern Recognition (CVPR) Workshops, Honolulu, HI, USA, 21–26 July 2017.
14. Liu, Y.; Guo, C.; Cao, J.; Cheng, Z.; Ding, X.; Lv, L.; Li, F.; Gong, M. A New Resolution Enhancement Method for Sandstone Thin-Section Images Using Perceptual GAN. *J. Pet. Sci. Eng.* **2020**, *195*, 107921. [CrossRef]
15. Wang, X.; Yu, K.; Wu, S.; Gu, J.; Liu, Y.; Dong, C.; Qiao, Y.; Loy, C.C. ESRGAN: Enhanced Super-Resolution Generative Adversarial Networks. In *Computer Vision—ECCV 2018 Workshops*; Leal-Taixé, L., Roth, S., Eds.; Lecture Notes in Computer Science; Springer International Publishing: Cham, Switzerland, 2019; Volume 11133, pp. 63–79. ISBN 978-3-030-11020-8.

16. Zhang, Y.; Tian, Y.; Kong, Y.; Zhong, B.; Fu, Y. Residual Dense Network for Image Super-Resolution. In Proceedings of the IEEE Conference on Computer Vision and Pattern Recognition (CVPR), Salt Lake City, UT, USA, 18–23 June 2018.
17. Vaswani, A.; Shazeer, N.; Parmar, N.; Uszkoreit, J.; Jones, L.; Gomez, A.N.; Kaiser, L.; Polosukhin, I. Attention Is All You Need. In Proceedings of the 31st Conferenceon Neura lInformation Processing Systems (NIPS2017), Long Beach, CA, USA, 4–9 December 2023.
18. Wang, H.; Chen, X.; Ni, B.; Liu, Y.; Liu, J. Omni Aggregation Networks for Lightweight Image Super-Resolution. In Proceedings of the IEEE/CVF Conference on Computer Vision and Pattern Recognition (CVPR), Vancouver, BC, Canada, 17–24 June 2023.
19. Hui, Z.; Wang, X.; Gao, X. Fast and Accurate Single Image Super-Resolution via Information Distillation Network. In Proceedings of the 2018 IEEE/CVF Conference on Computer Vision and Pattern Recognition, Salt Lake City, UT, USA, 18–23 June 2018; pp. 723–731.
20. Shi, W.; Caballero, J.; Huszár, F.; Totz, J.; Aitken, A.P.; Bishop, R.; Rueckert, D.; Wang, Z. Real-Time Single Image and Video Super-Resolution Using an Efficient Sub-Pixel Convolutional Neural Network. In Proceedings of the IEEE Conference on Computer Vision and Pattern Recognition (CVPR), Las Vegas, NV, USA, 27–30 June 2016.
21. Zhang, Y.; Li, K.; Li, K.; Wang, L.; Zhong, B.; Fu, Y. Image Super-Resolution Using Very Deep Residual Channel Attention Networks. In Proceedings of the European Conference on Computer Vision (ECCV), Munich, Germany, 8–14 September 2018.
22. Kirillov, A.; Mintun, E.; Ravi, N.; Mao, H.; Rolland, C.; Gustafson, L.; Xiao, T.; Whitehead, S.; Berg, A.C.; Lo, W.-Y.; et al. Segment Anything. In Proceedings of the IEEE/CVF International Conference on Computer Vision (ICCV), Paris, France, 2–3 October 2023.
23. Park, J.; Woo, S.; Lee, J.-Y.; Kweon, I.S. BAM: Bottleneck Attention Module. In Proceedings of the IEEE Conference on Computer Vision and Pattern Recognition (CVPR), Salt Lake City, UT, USA, 18–23 June 2018.
24. Woo, S.; Park, J.; Lee, J.-Y.; Kweon, I.S. CBAM: Convolutional Block Attention Module. In *Computer Vision—ECCV 2018*; Ferrari, V., Hebert, M., Sminchisescu, C., Weiss, Y., Eds.; Lecture Notes in Computer Science; Springer International Publishing: Cham, Switzerland, 2018; Volume 11211, pp. 3–19. ISBN 978-3-030-01233-5.
25. Hu, J.; Shen, L.; Albanie, S.; Sun, G.; Wu, E. Squeeze-and-Excitation Networks. In Proceedings of the IEEE Conference on Computer Vision and Pattern Recognition (CVPR), Salt Lake City, UT, USA, 18–23 June 2018.
26. Piao, Y.; Ji, W.; Li, J.; Zhang, M.; Lu, H. Depth-Induced Multi-Scale Recurrent Attention Network for Saliency Detection. In Proceedings of the 2019 IEEE/CVF International Conference on Computer Vision (ICCV), Seoul, Republic of Korea, 27 October–2 November 2019; pp. 7253–7262.
27. Dong, C.; Loy, C.C.; He, K.; Tang, X. Image Super-Resolution Using Deep Convolutional Networks. *IEEE Trans. Pattern Anal. Mach. Intell.* **2016**, *38*, 295–307. [CrossRef] [PubMed]
28. Shi, J.; Zhang, H. Adaptive Local Threshold with Shape Information and Its Application to Object Segmentation. In Proceedings of the 2009 IEEE International Conference on Robotics and Biomimetics (ROBIO), Guilin, China, 13–19 December 2009; pp. 1123–1128.

Disclaimer/Publisher's Note: The statements, opinions and data contained in all publications are solely those of the individual author(s) and contributor(s) and not of MDPI and/or the editor(s). MDPI and/or the editor(s) disclaim responsibility for any injury to people or property resulting from any ideas, methods, instructions or products referred to in the content.